International Journal of Biological Macromolecules 194 (2022) 110–116

Contents lists available at ScienceDirect

International Journal of Biological Macromolecules

journal homepage: www.elsevier.com/locate/ijbiomac

Synthesis, characterization and biocompatibility of guar gum-benzoic acid

Trung-Anh Le [a], Yong Guo [b,c,d], Jun-Nian Zhou [b,c,e], Jiaqi Yan [b,c], Hongbo Zhang [b,c], Tan-Phat Huynh [a,*]

[a] Laboratory of Molecular Science and Engineering, Faculty of Science and Engineering, Åbo Akademi University, Henrikinkatu 2, 20500 Turku, Finland
[b] Pharmaceutical Sciences Laboratory, Faculty of Science and Engineering, Åbo Akademi University, Porthaninkatu 3–5, 20500 Turku, Finland,
[c] Turku Bioscience Centre, University of Turku and Åbo Akademi University, Turku 20520, Finland
[d] Department of Endocrinology, Key Laboratory of National Health & Family Planning Commission for Male Reproductive Health, National Research Institute for Family Planning, Beijing 100081, China
[e] Experimental Hematology and Biochemistry Lab, Beijing Institute of Radiation Medicine, Beijing 100850, China

ARTICLE INFO

Keywords:
Guar gum
Benzoic acid
Nucleophilic substitution
Computational chemistry
Biocompatibility

ABSTRACT

A novel chemical functionalization of guar gum (GG) by benzoic acid (BA) via nucleophilic substitution reaction in aqueous solution has been reported. BA moieties are chosen due to coordination chemistry of carboxylic acid moieties, hydrophobicity and intermolecular interaction of aromatic rings. The presence of conjugated BA on guar gum-benzoic acid (GG-BA) with grafting density of 5.5% is confirmed by ^{1}H NMR. Amorphous GG-BA with irregular morphology has been studied by UV–Vis, FTIR, XRD, SEM, TEM, TGA, computational chemistry and contact angle measurement. GG-BA in a concentration range from 0 to 4000 μg mL^{-1} has good biocompatibility to mouse embryonic fibroblasts (MEF), human mammary epithelial cells (MCF-10A) after 48 and 72 h of treatment using WST-1 assay. GG-BA shows great potential for the development of biomaterials such as bioadhesives, hydrogels, and coacervates.

1. Introduction

Over the years, natural polysaccharides have been of great interest in developing valuable and sustainable materials due to their biocompatibility, nontoxicity, biodegradability, natural availability, and accessibility of chemical synthetic techniques [1,2]. Guar gum (GG), a naturally occurring non-ionic galactomannan polysaccharide obtained from guar seeds, has recently become a popular choice of novel materials research in various fields such as soil treatment [3–6], surface chemistry [7–9], lithium- and zinc-ion batteries [10,11], dye-sensitized solar cells [12], wound dressing and healing [13–15], drug delivery [16,17]. GG consists of mannose (M) backbones and galactose (G) side chains with an average molecular ratio of 2:1 between M and G. While M monomers are linked together by β-1,4-glycosidc bonds, G monomers are connected to the M backbone via α-1,6-glycosidic bonds. In addition, numerous remaining hydroxyl functional (-OH) groups on galactomannan chains offer GG its hydrophilicity and high water-solubility [18,19].

In order to introduce new properties to GG, remaining -OH groups of GG can be chemically functionalized by different chemical reactions such as etherification, esterification, oxidation, grafting reactions, etc.

Abbreviations: AGU, anhydroglucose unit; APFD, Austin-Frisch-Petersson functional with dispersion; BA, benzoic acid; BBA, 4-(bromomethyl)benzoic acid; CCD, charge-coupled device; DFT, density functional theory; DMEM, Dulbecco's modified eagle medium; DMEM/F12, Dulbecco's modified eagle medium/Nutrient mixture F-12; DMSO-d_6, deuterated dimethylsulfoxide; DS, degree of substitution; DSC, differential scanning calorimetry; DTG, derivative of weight loss; EGF, epidermal growth factor; ESP, electrostatic potential; FBS, Fetal bovine serum; FTIR-ATR, Fourier-transform infrared radiation-attenuated total reflectance; G, galactose; GG, guar gum; GG-BA, guar gum-benzoic acid; GD, grafting density; HOMO, highest occupied molecular orbitals; ^{1}H NMR, proton nuclear magnetic resonance; LED, light-emitting diode; LUMO, lowest unoccupied molecular orbitals; M, mannose; MCF-10A, human mammary epithelial cells; MEF, mouse embryonic fibroblasts; MO, molecular orbital; MOF, metal-organic frameworks; MW, molecular weight; -OH, hydroxyl; PBS, phosphate buffered saline; PCM, polarized continuum model; SCRF, self-consistent reaction field; SD, standard deviations; SEM, scanning electron microscopy; TD-DFT, time-dependent density functional theory; TEM, transmission electron microscopy; TGA, thermogravimetric analysis; UV–Vis, ultraviolet-visible; WST-1, 4-[3-(4-Iodophenyl)-2-(4-nitro-phenyl)-2H-5-tetrazolio]-1;3-benzene sulfonate; XRD, X-ray diffraction.

* Corresponding author at: Laboratory of Molecular Science and Engineering, Faculty of Science and Engineering, Åbo Akademi University, Henrikinkatu 2, 20500 Turku, Finland.

E-mail address: tan.huynh@abo.fi (T.-P. Huynh).

https://doi.org/10.1016/j.ijbiomac.2021.11.180
Received 28 March 2021; Received in revised form 2 November 2021; Accepted 26 November 2021
Available online 1 December 2021

Carboxymethylation of GG via ether bonds is one of the most common synthetic routes to synthesize anionic GG [20,21]. Further cross-linking of carboxymethylated GG can be easily carried out using non-covalent interactions by an assistance of multivalent metal ions [22–24]. Complex coacervation between carboxymethylated GG and cationic polymers such as gelatin has also been studied [25]. Moreover, esterification of -OH groups on GG was performed with citric acid to create cross-linked polymer systems for wound healing [14], while those -OH groups of GG could also form covalent bonds directly with several common cross-linkers such as Ti^{4+} and borate [5,26]. In addition, oxidation of -OH groups to aldehydes is also another option to functionalize and cross-link GG [27]. Even though GG possesses various fascinating properties, intrinsic limitations of GG remain due to its hydrophilicity, leading to uncontrollable swelling properties, as well as its susceptibility to bacterial contamination and rapid biodegradation. Chemical modification of GG is, therefore, of great importance to extend its applicability [28].

Benzoic acid (BA) and its derivatives have been well-known for their chelating capacity and various types of intermolecular interaction such as hydrogen bonding and π stacking [29–35]. BA derivatives, therefore, were widely used to synthesize numerous metal-organic frameworks (MOFs) [36–39] and recognize bioanalytes such as adrenaline and carnosine [40,41]. Moreover, BA can be found in various cosmetic products, medications and food as additives and preservatives to certain approved concentrations [42,43]. BA derivatives were also reported with beneficial antimicrobial, antifungal and antihepatotoxic activity [44–46].

This work aims to synergize GG with BA to offer novel properties based on the following hypotheses. Since BA contains a carboxylic acid functional group which might be deprotonated more readily than alcohol groups of GG, the anionic GG-BA could be more easily obtained at milder alkaline conditions once BA is conjugated to GG. With this ionic form, coordination compounds of GG-BA with various metal cations could also be explored effortlessly. In addition, the aromatic benzene ring on BA could decrease not only the hydrophilicity of GG, hence, overcoming the intrinsic hydrophilicity obstacles of GG, but also could assist the preparation of novel complex materials due to numerous intermolecular interaction that the aromatic benzene ring might offer. Moreover, because of the widely recognized biocompatibility, antimicrobial and antifungal activity of BA, the conjugation of GG with BA might enhance the material stability against bacterial contamination and biodegradation. In order to realize GG-BA, a simple synthetic protocol in water was established for the first time and the newly obtained product was characterized by various techniques such as ^{1}H NMR, UV–Vis, FTIR-ATR, XRD, SEM, TEM, contact angle and TGA-DSC. Computational chemistry was employed to provide valuable insights into electronic properties of GG-BA as well as its molecular orbital diagram and electronic transitions between molecular orbitals. The biocompatibility of GG-BA was confirmed in the study on mouse embryonic fibroblasts (MEF) and human mammary epithelial cells (MCF-10A) using WST-1 assay, which shows great potential for the development of biomaterials.

2. Materials and methods

2.1. Chemicals and reagents

2.1.1. Chemicals for synthesis

GG (MW = 220 kDa), 4-(bromomethyl)benzoic acid (BBA) 97%, sodium hydroxide (NaOH) 97%, hydrochloric acid (HCl) 37%, ethanol 98% (EtOH) and deuterated dimethylsulfoxide (DMSO-d_6) were purchased from Sigma-Aldrich. All chemicals were reagent-grade and used as received without further purification.

2.1.2. Chemicals for cell culture

Dulbecco's modified eagle medium (DMEM) and phosphate buffered saline (PBS) were purchased from Lonza. Fetal bovine serum (FBS), Dulbecco's modified eagle medium/Nutrient mixture F-12 (DMEM/F-12), Trypsin, L-glutamine, and Penicillin/Streptomycin were purchased from Gibco. Human insulin, hydrocortisone, cholera toxin and glucose were purchased from Sigma-Aldrich. Epidermal growth factor (EGF) from Peprotech and cell proliferation reagent WST-1 from Roche were also purchased. All reagents were cell-culture grade.

2.2. Synthesis and preparation

2.2.1. Guar gum benzoic acid (GG-BA)

5.00 g of GG (30.875 mmol AGU) and 5.73 g of NaOH (138.94 mmol, 4.5 eq) were dissolved in 500 mL N_2-purged H_2O and the solution was stirred in 30 min at room temperature. 6.845 g of BBA (30.875 mmol, 1 eq) was then added into the solution and the mixture was kept under magnetic stirring overnight at room temperature. HCl (37%) was added to quench the reaction and acidify the solution to pH 1. Excess EtOH was used to precipitate and purify GG-BA. The final product was dried in vacuum to yield 7.62 g of GG-BA (83.1% reaction yield).

2.3. Characterization

2.3.1. Proton nuclear magnetic resonance (^{1}H NMR) spectroscopy

^{1}H NMR spectra of samples were measured by Bruker AVANCE-III NMR-system 400 MHz (Bruker Inc., Billerica, MA, USA) at 298.15 K. Dry samples of GG and GG-BA were dissolved in DMSO-d_6 at 50 °C.

2.3.2. UV–Visible spectrophotometry

Solutions of all samples were prepared in H_2O at pH 1 and room temperature. UV–Vis spectra were measured in the range of 190 to 700 nm with a resolution of 0.5 nm, using Shimadzu UV-2501PC spectrophotometer (Shimadzu Inc., Kyoto, Japan) and quartz cuvettes.

2.3.3. Fourier-transform infrared spectroscopy - Attenuated total reflectance (FTIR-ATR) spectroscopy

Nicolet™ iS50 FTIR spectrometer (Thermo Scientific Inc., Waltham, MA, USA) equipped with a diamond crystal and a pressure gauge was used to record IR spectra. IR spectra were recorded in the wavenumber range of 400 to 4000 cm^{-1} with a resolution of 4.0 cm^{-1} and averaged from 64 scans.

2.3.4. Powder X-ray diffraction (XRD)

XRD spectra of GG and GG-BA were measured on Bruker D8 Discover (Bruker Inc., Billerica, MA, USA) diffractometer in a diffraction angle range between 10 to 80° and a resolution of 0.04° at room temperature. X-ray K780 (Cu Kα anode) generator was used at 40 kV voltage and 40 mA current.

2.3.5. Scanning electron microscopy (SEM)

LEO Gemini 1530 scanning electron microscope with thermo scientific ultradry silicon drift detector (Leo Electron Microscopy Inc., Thornwood, NY, USA) was used to study the morphology of GG and GG-BA samples. Samples were coated on conductive carbon adhesive tapes. Resultant SEM images were analysed and particle diameters were examined using Image J software. Particle size distribution curves were plotted based on 50 particles of GG and 150 particles of GG-BA.

2.3.6. Transmission electron microscopy (TEM)

JEM-1400 plus transmission electron microscope equipped with an OSIS Quemesa 11 Mpix bottom mounted digital camera (Jeol Ltd., Akishima, Tokyo, Japan) was also employed to characterize the morphology of GG and GG-BA samples. The acceleration voltage was kept at 80.00 kV, while the beam current was 55 μA. The samples were dispersed onto standard copper TEM grids and resultant TEM images were also analysed by Image J software.

2.3.7. Thermogravimetric analysis - differential scanning calorimetry (TGA-DSC)

Netzsch STA 449 F1 Jupiter thermogravimetric analyzer (Netzsch Instruments Inc., Featherstone, Wolverhampton, UK) was employed under N_2 inert atmosphere from 30 to 600 °C at a heating rate of 10 °C min^{-1}. N_2 flow rate was kept at 20 mL min^{-1}. Dry samples were kept in vacuum before the measurements and 2–10 mg of the dry samples were transferred to aluminium DSC pans. Resultant TGA, DTG, DSC curves were analysed by Netzsch TGA software.

2.3.8. Contact angle

Hydrophilicity and hydrophobicity of GG and GG-BA were studied by water static dripping contact angle experiments using a KSV CAM 200 Optical tensiometer (KSV Instruments Ltd., Helsinki, Finland) equipped with a LED light source and a CCD camera with telecentric zoom optics. FTIR hydraulic press was used to prepare 3 pellets of GG and 3 pellets of GG-BA under 10 t of pressure in 15 min for each sample (Fig. S8). For each pellet, 3 random locations were chosen to record the contact angles, hence, 9 measurements were carried out in total for GG and also for GG-BA. Small distilled water droplets of 2.0 μL were released on the film surface at the dispensing rate of 100 μL s^{-1}. Digital pictures were recorded automatically within 24 s for each measurement and CAM software using Young-Laplace fitting method was chosen to calculate the contact angles. From the right and left contact angles, average contact angles were calculated for each picture. The final average contact angles and standard deviations (SD) were then determined from those 9 measurements. The final average equilibrium contact angle was finally determined after 15 s when there was no significant change in the average contact angle values recorded (Fig. S11).

2.4. Computational study

All computational calculations were performed by Gaussian 16 program package. The geometry of all involved structures was fully optimized by the Austin-Frisch-Petersson (APFD) hybrid density functional theory (DFT) method with dispersion, combined with the 6–311+G(d,p) basis set [47]. The UV–Vis absorption wavelengths and oscillator strengths were calculated by means of time-dependent density functional theory (TD-DFT), using the same basis sets [48]. Molecular orbitals (MOs) and electrostatic potential maps of optimized geometry structures were calculated at the same level of theory and visualized using Gaussview 6 [49]. Solvent effects of water were evaluated by employing the self-consistent reaction field (SCRF) method with polarized continuum model (PCM) [50].

.

2.5. Biocompatibility study

2.5.1. Cell culture

Mouse embryonic fibroblasts (MEF) were cultured in DMEM (Lonza) containing 10% FBS (Gibco). Human normal breast cells (MCF-10A) were cultured in DMEM/F12 Medium (Gibco) containing 5% FBS (Gibco), 2 mM L-glutamine (Gibco), human insulin, (Sigma, 10 μg mL^{-1}), glucose (Sigma, 4.5 g L^{-1}), hydrocortisone (Sigma, 0.5 μg mL^{-1}), cholera toxin (Sigma, 0.1 μg mL^{-1}) and epidermal growth factor (EGF, Peprotech, 20 ng mL^{-1}), in a humidified incubator with 5% CO_2. MCF-10A cells were provided by Prof. Jukka Westermarck (Turku Bioscience Centre, Turku, Finland).

2.5.2. Biocompatibility study

MEF cells and MCF-10A cells were placed in a 96-well plate (three parallel wells for each concentration, Corning) at suitable starting cell density (3000 cells per well for 48 h-incubation of GG and GG-BA, and 2000 cells per well for 72 h-incubation of GG and GG-BA) in the complete growth medium at 37 °C, 5% CO_2 overnight. Then, the cell culture medium was replaced with a fresh medium containing GG or GG-BA at indicated concentrations (0–4000 μg mL^{-1}) for 48 h and 72 h. The GG and GG-BA solutions were prepared in PBS. For WST-1 assay, 10 μL of WST-1 reagent (Roche) was dissolved in 100 μL complete growth medium to replace the GG or GG-BA-contained medium for each well. After two-hour-incubation in cell incubator, the absorbance was measured at 440 nm with a Varioskan™ LUX Multimode Reader (Thermo Scientific Inc., Waltham, MA, USA). WST-1 cell viability data are presented as the means ± standard deviations.

3. Results and discussions

3.1. Synthesis of GG-BA

Hydroxyl groups of GG were first activated by NaOH and the reaction was carried out in aqueous condition at room temperature, which offered a convenient and environmental friendly synthetic route. Nucleophilic substitution was performed on BBA to yield ether chemical bonds between GG and BA moieties (Fig. 1). The original high-molecular-weight GG material has good solubility in H_2O and poor solubility in polar aprotic solvents such as dimethylsulfoxide (DMSO). Meanwhile, the purified GG-BA product shows good solubility in both H_2O and DMSO, indicating the presence of BA moieties in GG-BA.

3.2. Characterization and computational study of GG-BA

3.2.1. Proton nuclear magnetic resonance (^1H NMR)

^1H NMR analysis of purified GG-BA product was carried out to confirm the successful chemical functionalization of GG and to determine the degree of substitution of GG-BA (Fig. 1 and Section 1 in supplementary data). While a satisfactory ^1H NMR spectrum of the original GG in DMSO-d_6 could not be obtained due to low solubility of GG in DMSO (Fig. S2), the ^1H NMR spectrum of GG-BA in DMSO-d_6 was easily received. This confirms the existence of BA moieties, which are chemically linked to GG. Aliphatic protons of galactomannan backbone in GG-BA exhibit signals with chemical shifts (δ) ranging between 3.4 and 5.0 ppm. Meanwhile, ortho and meta protons from BA moieties in GG-BA are apparent in the aromatic δ range from 7.3 to 8.0 ppm with equal intensity. The recorded aromatic signals of GG-BA are consistent with chemical shifts of aromatic protons from BBA starting material (7.56 and 7.92 ppm, Fig. S1). Based on the intensity of aliphatic and aromatic protons from GG-BA, the degree of substitution of GG-BA is calculated as 0.1639, while the grafting density is 5.5% and the chemical formula for each anhydrous glucose unit (AGU) is approximated as $C_6H_{9.361}O_5(C_8H_7O_2)_{0.1639}$.

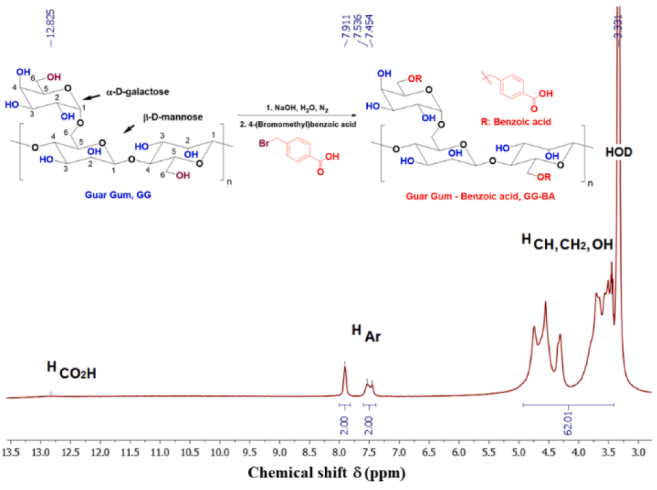

Fig. 1. ^1H NMR spectrum of GG-BA in DMSO-d_6.

3.2.2. UV–Vis spectrophotometry

Normalized UV–Vis absorption spectra of GG-BA, GG and BBA references were recorded from 190 to 700 nm in water at pH 1 (Fig. 2a). GG absorbs a wide range of UV–Vis radiation with two absorption maxima at 341.0 and 262.0 nm. Its UV absorption expands drastically towards 190 nm. BBA shows no significant absorption band in the visible range, while a major absorption maximum at 246.5 nm as well as a small absorption band around 290.0 nm are recorded. Similarly to BBA, GG-BA also exhibits no noticeable absorption band in the visible range, but similar absorption bands to BBA in the middle-UV region between 200 and 300 nm. Since the galactomannan backbone and BA moieties of GG-BA have different molar absorption coefficients, as well as almost no absorption band in the visible range is observed, the UV–Vis spectrum of GG-BA can be mainly attributed to the UV–Vis absorption of the newly introduced BA moieties. Comparing to BBA, the absorption maximum of GG-BA spectrum is blue-shifted from 246.5 nm to 236.5 nm. In addition, a small absorption band around 280 nm of GG-BA might be due to either the blue-shifted absorption of BA moieties or the absorption of galactomannan backbone.

3.2.3. Computational study on electronic properties

In an effort of correlating electronic transitions in GG-BA and its experimental UV–Vis absorption data, DFT calculation using APFD/6311+G(d) has been used to model a monomer of GG-BA and study its electronic properties [47]. This is because APFD, including treatments of dispersion effects, represents the best trade-off between accuracy and computational cost for a relatively large system such as GG-BA. Together with 6311+G(d), the model provides good accuracy while being feasible for use on typical computer workstations. The calculation was performed in the presence of water (using SCRF keyword) to mimic the aqueous condition of the UV–Vis measurements. The optimized structure and electrostatic potential (ESP) surface of GG-BA monomer are shown in Fig. 2c and S3. Theoretical UV–Vis absorption spectra of BBA reference and GG-BA monomer (Fig. 2b) were calculated by TD-DFT method to reach a good agreement with the experimental UV–Vis spectra (i.e., calculated absorption maxima at 238.3 and 252.7 nm of GG-BA monomer and BBA, comparing to 236.5 and 246.5 nm for experimental GG-BA and BBA respectively). The calculated UV–Vis absorption band around 238.3 nm of GG-BA monomer is composed of five different electronic transitions from highest occupied molecular orbitals HOMO-4, HOMO-3, HOMO-2, HOMO-1 and HOMO to lowest unoccupied molecular orbitals LUMO. The calculated HOMO-LUMO energy gap of GG-BA monomer is determined as 5.260 eV, which corresponds to 235.7 nm (Fig. 2d). The slight difference between 235.7 and 238.3 nm is due to electronic effect of water solvent and this also indicates that the HOMO-LUMO electronic transition contributes mainly to the absorption maximum of GG-BA monomer at around 238.3 nm. Moreover, a blue shift in the wavelength of absorption maxima is also observed in the calculated spectra. The MO diagram of GG-BA monomer from HOMO-4 to LUMO+2 can be found in Fig. S4.

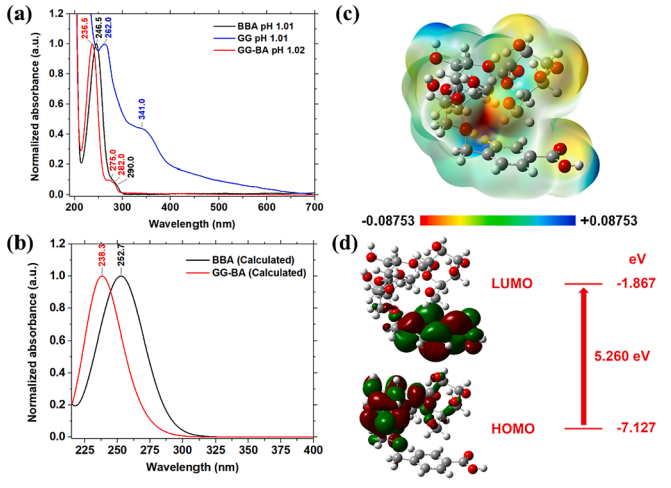

Fig. 2. Experimental (a) and calculated (b) UV–Vis absorption spectra of BBA, GG and GG-BA in water at pH 1. The optimized structure and ESP surface of GG-BA monomer (c) and its HOMO-LUMO gap and MO visualizations (d).

3.2.4. Fourier-transform infrared spectroscopy (FTIR)

FTIR spectra of original GG and GG-BA were measured to show that typical IR absorption bands of galactomannan backbone can be observed in both spectra (Fig. 3a). The O—H stretching vibration with intermolecular hydrogen bonding can be found in the wavenumber range between 3000 and 3500 cm^{-1}, followed by C—H stretching of CH_2 group with wavenumber between 2800 and 3000 cm^{-1}. The absorption band of 1645 cm^{-1} is due to ring stretching while strong absorption peaks of 1143, 1065 and 1012 cm^{-1} show C-OH bond, CH_2OH stretching and CH_2 twisting vibrations, respectively. A typical peak of 867 cm^{-1} for galactose and mannose is also observed [51–53]. By comparing IR spectra of GG and GG-BA, the presence of BA moieties in GG-BA can be confirmed. The characteristic C═O stretching absorption band from carboxylic acid groups of GG-BA appears at 1694 cm^{-1}, which is similar to the C═O stretching absorption band of BBA reference at 1678 cm^{-1} (Fig. S5). The C—O stretching vibration from carboxylic acid groups is also observed in GG-BA spectrum at 1255 cm^{-1}, while the IR spectrum of BBA reference shows a strong absorption band for that type of vibration at 1287 cm^{-1} (Fig. S5). The O—H stretching vibration wavenumber of hydroxyl functional groups shifts from 3330 to 3358 cm^{-1}, indicating an increase in the O—H bond strength of GG-BA. This can be explained as the intermolecular hydrogen bonding strength in GG-BA decreases, comparing to that of GG, due to the presence of hydrophobic BA moieties [54].

3.2.5. X-ray diffractometry (XRD)

Fig. 3b shows X-ray diffractograms of GG and GG-BA. Both materials possess broad peaks at similar 2θ values of 17.84, 18.36, 43.12 and 43.72°, showing amorphous phase structure of GG and GG-BA. The slightly broader peak of GG-BA at 18.36° indicates smaller particle size and/or lower crystallinity of GG-BA particles.

3.2.6. Scanning electron microscopy (SEM) and transmission electron microscopy (TEM)

Fig. 4 shows scanning electron micrographs and particle size distribution curves of GG and GG-BA particles. SEM images of GG were not easily obtained since GG has low electrical conductivity, while it was easier to record SEM images for GG-BA. Both GG and GG-BA particles have irregular shapes. To determine the particle size, the shape of particles is approximated as spherical. The particle size distribution is then fitted by Gaussian functions to give average diameters of GG and GG-BA as 637 ± 16 nm and 196 ± 17 nm respectively. In addition, transmission electron micrographs show slightly smaller particle size, of around 400 to 600 nm for GG and around 100 to 200 nm for GG-BA (Figs. S6–7), comparing to SEM images. However, TEM still confirms a smaller particle size of GG-BA comparing to that of GG. The significant changes in

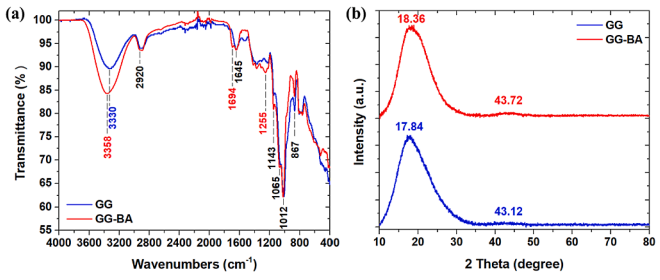

Fig. 3. FTIR spectra of GG and GG-BA (a). XRD spectra of GG and GG-BA (b).

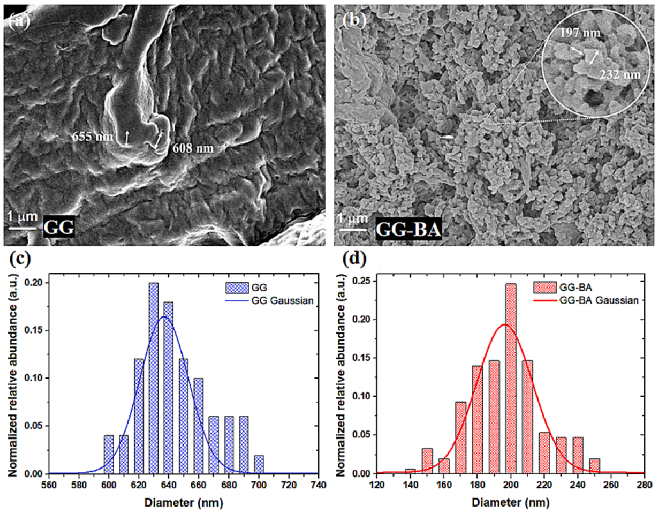

Fig. 4. SEM images (a, b) and particle size distribution curves (c, d) of GG and GG-BA.

particle size between GG and GG-BA can be explained due to the dissolution of GG in water and precipitation of GG-BA product by ethanol during the chemical functionalization.

3.2.7. Contact angle

Static contact angles of distilled water droplets on film surface of GG and GG-BA were measured to study the effect of BA on a decrease in hydrophilicity of GG-BA comparing to GG. In general, contact angles can be correlated to surface energy and roughness, hence, surface wettability and hydrophobicity of materials. The larger the contact angle, the lower the surface energy and higher the surface roughness, resulting in the lower wettability, lower hydrophilicity or higher hydrophobicity of a surface. Hydrophilic, hydrophobic and superhydrophobic surfaces typically have water contact angles of less than 90°, greater than 90° and above 150°, respectively [55–57]. Fig. S9 shows water contact angles on a representative GG reference film. In the first 10 s, contact angles of water on GG are recorded of around 90° on average, which is contradictory to the hydrophilic nature and high water-solubility of GG. In the next 14 s, GG quickly moves from the film surface into the water droplet and starts swelling, hence, contact angles of GG cannot be determined eventually. The same phenomenon is observed in all 9 repetitive measurements on GG. This could be because GG were pressed very strongly into solid films during the sample preparation, therefore, water wetting on the hydrophilic GG surface cannot be established immediately. Then, due to the strong interaction between hydrophilic GG and water droplet, the GG area, which is in direct contact with water, is quickly softened and GG can move from the film to the water droplet. Regarding GG-BA, contact angles of water on GG-BA film surface are well established during 24 s of measurement, in the range between 70 and 60° (Fig. S10). The surface of GG-BA film remains stable during all the measurements and the average equilibrium contact angle of water on GG-BA is determined as 66.0° (Fig. S11), suggesting that GG-BA is still mainly hydrophilic. Based on the observations from these contact angle measurements and the solubility of GG and GG-BA in water and DMSO from NMR measurements (Section 3.2.1), the presence of BA conjugated to GG (GG-BA) can be associated with the decrease in hydrophilicity of GG-BA comparing to GG.

3.2.8. Thermal analysis

In order to study thermal properties of GG and newly prepared GG-BA, TGA-DSC measurements were performed. TGA, DSC and derivative of weight loss (DTG) thermograms of the two materials are shown in Fig. 5a, b. An initial weight loss due to water desorption is observed on

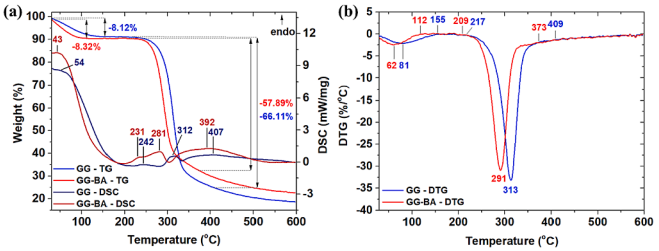

Fig. 5. TGA, DSC thermograms (a) and DTG thermograms (b) of GG and GG-BA in N_2.

DTG at around 62 and 81 °C for GG-BA and GG, respectively. While GG shows a gradual weight loss of 8.12% as the temperature reaches 155 °C, a weight loss of 8.32% of GG-BA is complete at a lower temperature, of around 112 °C. Moreover, DSC curves also show large endothermic peaks for water evaporation processes at temperature less than 200 °C. These DTG, TGA and DSC results are consistent with the previous observations on the decrease in hydrophilicity and the decrease in intermolecular hydrogen bonding of GG-BA due to chemically linked BA groups on GG. Thermal decomposition of galactomannan chains occurs in the temperature range from 209 to 373 and from 217 to 409 °C for GG-BA and GG, with the largest weight loss at 291 and 313 °C based on DTG, respectively. These decomposition temperature ranges are characteristic for galactomannan polysaccharides in N_2 inert atmosphere [51]. In addition, DSC thermograms show three endothermic events at around 231, 281, 392 °C for GG-BA and 242, 312, 407 °C for GG. Temperature and enthalpy values of thermodynamic events of GG and GG-BA are summarized in Table 1. Even though the thermal decomposition of GG-BA happens at a lower temperature range than that of GG, a smaller weight loss of 57.89% is observed in GG-BA while 66.11% is the weight loss of GG from TGA thermograms. This might be due to the smaller grain size of GG-BA comparing to that of GG, resulting in higher surface area of GG-BA particles. The higher surface area allows a much faster and more efficient heat transfer process, hence, lowering the decomposition temperature range of GG-BA.

3.3. Biocompatibility of GG-BA

As mesenchymal and epithelial cells are the two main types of cells that consist of tissues and organs, the most widely used MEF and MCF-10A were chosen to examine the biocompatibility of GG-BA. WST-1-based colorimetric assay is widely used in the detection of cell proliferation, survival and cytotoxicity after drug and biological material treatments on cells [58–60]. The working principle of the assay is based on the conversion of the light-red tetrazolium salt WST-1 (added earlier to the cell culture medium) into the dark-red formazan by the electron coupling reagent and mitrochondrial succinate-tetrazolium-reductase system in the cell mitochondria. Within a certain concentration range, the absorbance of the solution and the cell survival is positively correlated. In this study, a concentration range from 0 to 4000 μg mL^{-1} for GG-BA together with GG as a control was examined. The obtained values were then standardized by untreated cells (concentration = 0). Fig. 6 shows that after 48 h of treatment up to 4000 μg mL^{-1}, both GG and GG-

Table 1
Temperature and enthalpy values of GG and GG-BA from DSC in N_2.

Sample	Peak number	Onset (°C)	T (°C)	Endset (°C)	ΔH (J g^{-1})
GG	1	30	54	204	+785.5
	2	221	242	277	+7.3
	3	285	312	331	+29.2
	4	335	407	585	+149.5
GG-BA	1	30	43	194	+710.3
	2 + 3	202	231, 281	301	+61.2
	4	305	392	537	+193.4

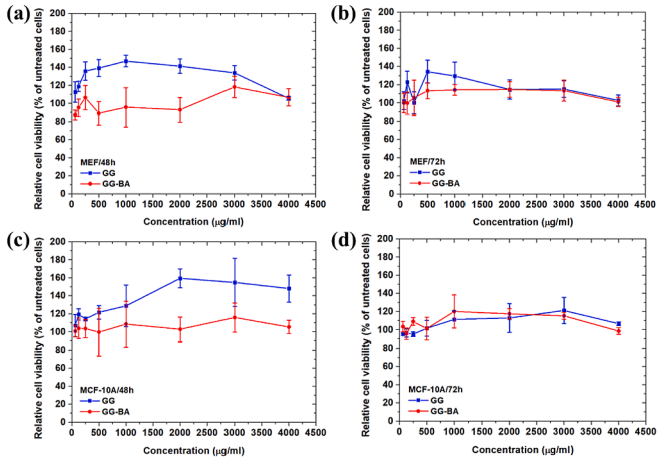

Fig. 6. Relative cell viability of MEF (a, b) and MCF-10A (c, d) cells treated with GG and GG-BA after 48 and 72 h. The cell viability in each group is normalized to untreated cells by percentage (%).

BA show no cytotoxicity to the two cell types, and GG has a stronger effect on promoting cell proliferation than GG-BA. After 72 h of treatment, the promotion effects of GG and GG-BA on the two kinds of cells appear to be the same, and still no cytotoxicity effect is observed. These results strongly indicate that GG-BA has good biocompatibility to normal mesenchymal cells and epithelial cells. Optical micrographs of cell studies can be found in the supplementary data (Figs. S12–16).

4. Conclusions

In this study, GG has been successfully chemically functionalized with BA moieties to give novel GG-BA materials for the first time. The reported synthetic route in water is simple and environmentally friendly since organic solvents are avoided. Due to the presence of benzene rings, the solubility of GG-BA product in polar aprotic solvents such as DMSO increases noticeably. This allows a straightforward characterization of GG-BA using ^{1}H NMR in DMSO-d_6. Other spectroscopic techniques such as UV–Vis and FTIR spectroscopies also confirm the presence of BA in GG-BA. XRD shows amorphous phase structure of both GG and GG-BA. SEM shows irregular shapes of GG and GG-BA, as well as a significant decrease in particle size of GG-BA. Contact angle measurements and the increase in solubility of GG-BA in DMSO indicate a decrease in hydrophilicity of GG-BA comparing to that of GG. TGA-DSC in N_2 atmosphere shows a lower thermal decomposition temperature and a smaller weight loss of GG-BA comparing to those of GG. Computational study on GG-BA shows good agreements with experimental data and gives a better understanding on the electronic properties of GG-BA. As GG-BA has shown good biocompatibility to living cells together with its rich coordination chemistry of benzoic acid moieties, GG-BA, therefore, is an excellent starting material for the development of new biomaterials such as hydrogels and coacervates for wound dressing, drug delivery, as well as bioadhesives.

Funding

Academy of Finland, Sigrid Jusélius Foundation.

CRediT authorship contribution statement

T.-A.L.: Conceptualization, Methodology, Investigation, Writing - Original Draft, Writing - Review & Editing. Y.G.: Methodology, Investigation, Writing - Review & Editing. J.-N.Z.: Methodology, Investigation, Writing - Review & Editing. H.Z.: Methodology, Writing - Review & Editing. T.-P.H.: Conceptualization, Supervision, Writing - Review & Editing, Project administration.

Declaration of competing interest

All authors reviewed and approved the final manuscript. The authors declare that they have no known competing financial interests or personal relationships that could have appeared to influence the work reported in this paper.

Acknowledgement

T.-A.L. acknowledges the DNMR doctoral fellowship from Åbo Akademi University. T.-P.H. would like to acknowledge the financial support from the starting fund from the Liv och Hälsa Foundation, and the Academy of Finland (Grant No. 323240). Y.G. and J.-N.Z. acknowledge the program of China Scholarships Council (No. 201909110009 and No. 201803170073). H.Z. acknowledges Academy of Finland (Grant No. 328933) and Sigrid Jusélius Foundation (decision no. 28002247K1) for financial support. Imaging/Flow cytometry was performed at the Cell Imaging and Cytometry core at Turku Bioscience Centre, which is supported by Biocenter Finland.

Appendix A. Supplementary data

Supplementary data to this article can be found online at https://doi.org/10.1016/j.ijbiomac.2021.11.180.

References

[1] B. Maji, 1 - Introduction to natural polysaccharides, in: S. Maiti, S. Jana (Eds.), Functional Polysaccharides for Biomedical Applications, Woodhead Publishing, 2019, pp. 1–31.
[2] F.G. Torres, O.P. Troncoso, A. Pisani, F. Gatto, G. Bardi, Natural polysaccharide nanomaterials: an overview of their immunological properties, Int. J. Mol. Sci. 20 (20) (2019) 5092.
[3] M.V.G. Paixão, R.D.C. Balaban, Application of guar gum in brine clarification and oily water treatment, Int. J. Biol. Macromol. 108 (2018) 119–126.
[4] E.R. Sujatha, S. Sivaraman, A.K. Subramani, Impact of hydration and gelling properties of guar gum on the mechanism of soil modification, Arab. J. Geosci. 13 (23) (2020) 1278.
[5] N. Thombare, U. Jha, S. Mishra, M.Z. Siddiqui, Borax cross-linked guar gum hydrogels as potential adsorbents for water purification, Carbohydr. Polym. 168 (2017) 274–281.
[6] N. Thombare, S. Mishra, M.Z. Siddiqui, U. Jha, D. Singh, G.R. Mahajan, Design and development of guar gum based novel, superabsorbent and moisture retaining hydrogels for agricultural applications, Carbohydr. Polym. 185 (2018) 169–178.
[7] C. Banerjee, S. Ghosh, G. Sen, S. Mishra, P. Shukla, R. Bandopadhyay, Study of algal biomass harvesting using cationic guar gum from the natural plant source as flocculant, Carbohydr. Polym. 92 (1) (2013) 675–681.
[8] B.S. Gupta, J.E. Ako, Application of guar gum as a flocculant aid in food processing and potable water treatment, Eur. Food Res. Technol. 221 (6) (2005) 746–751.
[9] A. Nakamura, M. Ozaki, K. Murakami, Elucidation of the aggregation mechanism of bentonite with cationic guar gum as flocculant and application to filtration, Colloids Surf. A Physicochem. Eng. Asp. 596 (2020), 124660.
[10] D.V. Carvalho, N. Loeffler, M. Hekmatfar, A. Moretti, G.-T. Kim, S. Passerini, Evaluation of guar gum-based biopolymers as binders for lithium-ion batteries electrodes, Electrochim. Acta 265 (2018) 89–97.
[11] Y. Huang, J. Zhang, J. Liu, Z. Li, S. Jin, Z. Li, H. Zhou, Flexible and stable quasi-solid-state zinc ion battery with conductive guar gum electrolyte, Mater. Today Energy 14 (2019), 100349.
[12] A. Gunasekaran, A. Sorrentino, A.M. Asiri, S. Anandan, Guar gum-based polymer gel electrolyte for dye-sensitized solar cell applications, Sol. Energy 208 (2020) 160–165.
[13] M.U.A. Khan, M.A. Raza, S.I.A. Razak, M.R. Abdul Kadir, A. Haider, S.A. Shah, S. Aftab, Novel functional antimicrobial and biocompatible arabinoxylan/guar gum hydrogel for skin wound dressing applications, J. Tissue Eng. Regen. Med. 14 (10) (2020) 1488–1501.
[14] P. Orsu, S. Matta, Fabrication and characterization of carboxymethyl guar gum nanocomposite for application of wound healing, Int. J. Biol. Macromol. 164 (2020) 2267–2276.
[15] R.R. Palem, K. Madhusudana Rao, T.J. Kang, Self-healable and dual-functional guar gum-grafted-polyacrylamidoglycolic acid-based hydrogels with nano-silver for wound dressings, Carbohydr. Polym. 223 (2019), 115074.
[16] S. Das, D. Bera, K. Pal, D. Mondal, P. Karmakar, S. Das, A. Dey, Guar gum micro-vehicle mediated delivery strategy and synergistic activity of thymoquinone and piperine: an in vitro study on bacterial and hepatocellular carcinoma cells, J. Drug Delivery Sci. Technol. 60 (2020), 101994.

[17] S. Sharma, S. Afgan, Deepak, A. Kumar, R. Kumar, l-Alanine induced thermally stable self-healing guar gum hydrogel as potential drug vehicle for sustained release of hydrophilic drug, Mater. Sci. Eng. C 99 (2019) 1384–1391.
[18] A. George, P.A. Shah, P.S. Shrivastav, Guar gum: versatile natural polymer for drug delivery applications, Eur. Polym. J. 112 (2019) 722–735.
[19] G. Sharma, S. Sharma, A. Kumar, A.A.H. Al-Muhtaseb, M. Naushad, A.A. Ghfar, F. J. Stadler, Guar gum and its composites as potential materials for diverse applications: a review, Carbohydr. Polym. 199 (2018) 534–545.
[20] G. Dodi, D. Hritcu, M.I. Popa, Carboxymethylation of guar gum: synthesis and characterization, Cellul. Chem. Technol. 45 (2011) 171–176.
[21] H. Gong, M. Liu, J. Chen, F. Han, C. Gao, B. Zhang, Synthesis and characterization of carboxymethyl guar gum and rheological properties of its solutions, Carbohydr. Polym. 88 (3) (2012) 1015–1022.
[22] W. Chen, Y. Bu, D. Li, Y. Liu, G. Chen, X. Wan, N. Li, Development of high-strength, tough, and self-healing carboxymethyl guar gum-based hydrogels for human motion detection, J. Mater. Chem. C 8 (3) (2020) 900–908.
[23] T. Reddy, S. Tammishetti, Gastric resistant microbeads of metal ion cross-linked carboxymethyl guar gum for oral drug delivery, J. Microencapsul. 19 (3) (2002) 311–318.
[24] R. Singh, S. Maity, B. Sa, Effect of ionic crosslink on the release of metronidazole from partially carboxymethylated guar gum tablet, Carbohydr. Polym. 106 (2014) 414–421.
[25] R.T. Thimma, S. Tammishetti, Study of complex coacervation of gelatin with sodium carboxymethyl guar gum: microencapsulation of clove oil and sulphamethoxazole, J. Microencapsul. 20 (2) (2003) 203–210.
[26] W. Xie, Z. Song, Z. Liu, X. Qian, Surface modification of PCC with guar gum using organic titanium ionic crosslinking agent and its application as papermaking filler, Carbohydr. Polym. 150 (2016) 114–120.
[27] L. Dai, L. Zhang, B. Wang, B. Yang, I. Khan, A. Khan, Y. Ni, Multifunctional self-assembling hydrogel from guar gum, Chem. Eng. J. 330 (2017) 1044–1051.
[28] R.R. Palem, G. Shimoga, K.S.V.K. Rao, S.-H. Lee, T.J. Kang, Guar gum graft polymer-based silver nanocomposite hydrogels: synthesis, characterization and its biomedical applications, J. Polym. Res. 27 (3) (2020) 68.
[29] K.V. Korpany, D.D. Majewski, C.T. Chiu, S.N. Cross, A.S. Blum, Iron oxide surface chemistry: effect of chemical structure on binding in benzoic acid and catechol derivatives, Langmuir 33 (12) (2017) 3000–3013.
[30] P. McArdle, Y. Hu, A. Lyons, R. Dark, Predicting and understanding crystal morphology: the morphology of benzoic acid and the polymorphs of sulfathiazole, CrystEngComm 12 (10) (2010) 3119–3125.
[31] L. Moreno-Gómez, F. Sánchez-Férez, T. Calvet, M. Font-Bardia, J. Pons, Zn(II) and Cd(II) monomer, dimer and polymer compounds coordinated by benzoic acid and 4-acetylpyridine: synthesis and crystal structures, Inorg. Chim. Acta 506 (2020), 119561.
[32] F. Qin, Y. Ma, L. Miao, Z. Wang, L. Gan, Influence of metal-ligand coordination on the elemental growth and alloying composition of Pt–Ni octahedral nanoparticles for oxygen reduction electrocatalysis, ACS Omega 4 (5) (2019) 8305–8311.
[33] C.V.K. Sharma, K. Panneerselvam, T. Pilati, G.R. Desiraju, Molecular recognition involving an interplay of O-H···O, C–H···O and π···π interactions. The anomalous crystal structure of the 1: 1 complex 3,5-dinitrobenzoic acid–4-(N, N-dimethylamino)benzoic acid, J. Chem. Soc. Perkin Trans. 2 (11) (1993) 2209–2216.
[34] W. Tang, M. Zhang, H. Mo, J. Gong, J. Wang, T. Li, Higher-order self-assembly of benzoic acid in solution, Cryst. Growth Des. 17 (10) (2017) 5049–5053.
[35] C.R. Vestal, Z.J. Zhang, Effects of surface coordination chemistry on the magnetic properties of MnFe2O4 spinel ferrite nanoparticles, J. Am. Chem. Soc. 125 (32) (2003) 9828–9833.
[36] R.A. Agarwal, N.K. Gupta, CO2 sorption behavior of imidazole, benzimidazole and benzoic acid based coordination polymers, Coord. Chem. Rev. 332 (2017) 100–121.
[37] K.P. Carter, J.A. Ridenour, M. Kalaj, C.L. Cahill, A thorium metal-organic framework with outstanding thermal and chemical stability, Chem. Eur. J. 25 (29) (2019) 7114–7118.
[38] M. Jahan, Q. Bao, J.-X. Yang, K.P. Loh, Structure-directing role of graphene in the synthesis of Metal−Organic framework nanowire, J. Am. Chem. Soc. 132 (41) (2010) 14487–14495.
[39] S. Yuan, T.-F. Liu, D. Feng, J. Tian, K. Wang, J. Qin, H.-C. Zhou, A single crystalline porphyrinic titanium metal–organic framework, Chem. Sci. 6 (7) (2015) 3926–3930.
[40] T.-P. Huynh, K.C.C. Bikram, W. Lisowski, F. D'Souza, W. Kutner, Molecularly imprinted polymer of bis(2,2′-bithienyl)methanes for selective determination of adrenaline, Bioelectrochemistry 93 (2013) 37–45.
[41] A. Wojnarowicz, P.S. Sharma, M. Sosnowska, W. Lisowski, T.-P. Huynh, M. Pszona, W. Kutner, An electropolymerized molecularly imprinted polymer for selective carnosine sensing with impedimetric capacity, J. Mater. Chem. B 4 (6) (2016) 1156–1165.
[42] J.R. Chipley, Sodium benzoate and benzoic acid, in: P.M. Davidson, A.L. Branen (Eds.), Antimicrobialsin Foods, Marcel Dekker, New York, 1993, pp. 11–48.
[43] W. Johnson, W.F. Bergfeld, D.V. Belsito, R.A. Hill, C.D. Klaassen, D.C. Liebler, F. A. Andersen, Safety assessment of benzyl alcohol, benzoic acid and its salts, and benzyl benzoate, Int. J. Toxicol. 36 (3_suppl) (2017) 5S–30S.
[44] B.-E. Amborabé, P. Fleurat-Lessard, J.-F. Chollet, G. Roblin, Antifungal effects of salicylic acid and other benzoic acid derivatives towards eutypa lata: structure–activity relationship, Plant Physiol. Biochem. 40 (12) (2002) 1051–1060.
[45] C. Gadgoli, S.H. Mishra, Antihepatotoxic activity of p-methoxy benzoic acid from Capparis spinosa, J. Ethnopharmacol. 66 (2) (1999) 187–192.
[46] E.-S. Park, W.-S. Moon, M.-J. Song, M.-N. Kim, K.-H. Chung, J.-S. Yoon, Antimicrobial activity of phenol and benzoic acid derivatives, Int. Biodeterior. Biodegrad. 47 (4) (2001) 209–214.
[47] A. Austin, G.A. Petersson, M.J. Frisch, F.J. Dobek, G. Scalmani, K. Throssell, A density functional with spherical atom dispersion terms, J. Chem. Theory Comput. 8 (12) (2012) 4989–5007.
[48] C. Adamo, D. Jacquemin, The calculations of excited-state properties with time-dependent density functional theory, Chem. Soc. Rev. 42 (3) (2013) 845–856.
[49] R. Dennington, T.A. Keith, J.M. Millam, GaussView, Version 6.1, Semichem Inc, Shawnee Mission, KS, 2016.
[50] G. Scalmani, M.J. Frisch, Continuous surface charge polarizable continuum models of solvation. I. General formalism, J. Chem. Phys. 132 (11) (2010), 114110.
[51] M.A. Cerqueira, B.W.S. Souza, J. Simões, J.A. Teixeira, M.R.M. Domingues, M. A. Coimbra, A.A. Vicente, Structural and thermal characterization of galactomannans from non-conventional sources, Carbohydr. Polym. 83 (1) (2011) 179–185.
[52] Z. Movasaghi, S. Rehman, D.I. ur Rehman, Fourier Transform Infrared (FTIR) spectroscopy of biological tissues, Appl. Spectrosc. Rev. 43 (2) (2008) 134–179.
[53] D. Mudgil, S. Barak, B.S. Khatkar, X-ray diffraction, IR spectroscopy and thermal characterization of partially hydrolyzed guar gum, Int. J. Biol. Macromol. 50 (4) (2012) 1035–1039.
[54] R.M. Silverstein, F.X. Webster, D.J. Kiemle, D.L. Bryce, Spectrometric Identification of Organic Compounds, 8th ed., Wiley, NJ, USA, 2014.
[55] K. Jayaramulu, F. Geyer, A. Schneemann, Š. Kment, M. Otyepka, R. Zboril, R. A. Fischer, Hydrophobic metal-organic frameworks, Adv. Mater. 31 (32) (2019) 1900820.
[56] K.-Y. Law, Definitions for hydrophilicity, hydrophobicity, and superhydrophobicity: getting the basics right, J. Phys. Chem. Lett. 5 (4) (2014) 686–688.
[57] K.L. Menzies, L. Jones, The impact of contact angle on the biocompatibility of biomaterials, Optom. Vis. Sci. 87 (6) (2010) 387–399.
[58] R. Kanchanapally, S. Deshmukh, S. Chavva, N. Tyagi, S. Srivastava, G. Patel, S. Singh, Drug-loaded exosomal preparations from different cell types exhibit distinctive loading capability, yield, and antitumor efficacies: a comparative analysis, Int. J. Nanomedicine 14 (2019) 531–541.
[59] I. Salcedo, C. Aguzzi, G. Sandri, M.C. Bonferoni, M. Mori, P. Cerezo, C. Caramella, In vitro biocompatibility and mucoadhesion of montmorillonite chitosan nanocomposite: a new drug delivery, Appl. Clay Sci. 55 (2012) 131–137.
[60] H. Tominaga, M. Ishiyama, F. Ohseto, K. Sasamoto, T. Hamamoto, K. Suzuki, M. Watanabe, A water-soluble tetrazolium salt useful for colorimetric cell viability assay, Anal. Commun. 36 (2) (1999) 47–50.